Chapter 9

Time-Frequency Analysis in Terahertz-Pulsed Imaging

Elizabeth Berry[1], Roger D Boyle[2], Anthony J Fitzgerald[3], and James W Handley[4]

[1] Academic Unit of Medical Physics, University of Leeds, `e.berry@leeds.ac.uk`
[2] School of Computing, Centre of Medical Imaging Research `roger@comp.leeds.ac.uk`
[3] Teraview Ltd., Cambridge, UK `tony.fitzgerald@teraview.co.uk`
[4] School of Computing, Centre of Medical Imaging Research `jwh@comp.leeds.ac.uk`

Summary. Recent advances in laser and electro-optical technologies have made the previously underutilized terahertz frequency band of the electromagnetic spectrum accessible for practical imaging. Applications are emerging, notably in the biomedical domain. In this chapter the technique of terahertz-pulsed imaging is introduced in some detail. The need for special computer vision methods, which arises from the use of pulses of radiation and the acquisition of a time series at each pixel, is described. The nature of the data is a challenge since we are interested not only in the frequency composition of the pulses, but also how these differ for different parts of the pulse. Conventional and short-time Fourier transforms and wavelets were used in preliminary experiments on the analysis of terahertz-pulsed imaging data. Measurements of refractive index and absorption coefficient were compared, wavelet compression assessed, and image classification by multi dimensional clustering techniques demonstrated. It is shown that the time-frequency methods perform as well as conventional analysis for determining material properties. Wavelet compression gave results that were robust through compressions that used only 20% of the wavelet coefficients. It is concluded that the time-frequency methods hold great promise for optimizing the extraction of the spectroscopic information contained in each terahertz pulse, for the analysis of more complex signals comprising multiple pulses or from recently introduced acquisition techniques.

9.1 Introduction

The terahertz (110 GHz to 10 THz) band of the electromagnetic spectrum, between microwaves and the infrared, has until recently been unexplored as a significant imaging tool. Recent advances in laser and electro-optical technologies now make the band accessible for practical use, and applications, notably in the medical domain, are emerging. Previously, terahertz radiation

was generated either by using thermal sources that produced weak and incoherent radiation, as conventionally used in far infrared Fourier transform spectroscopy, or by highly complex and bulky equipment such as free electron lasers or optically pumped gas lasers [1, 2]. Similarly, incoherent detection methods were used, which were able to record only the intensity of the terahertz electric field. The most sensitive detectors of this type were liquid helium cooled bolometers, which give a relatively noisy signal and have low sensitivity. The key advances that have made terahertz imaging a practical proposition have been in the fields of ultrashort pulsed lasers, nonlinear optics and crystal growth techniques [3]. These have resulted in sources of bright, coherent, broadband terahertz pulses and enabled coherent room temperature detection [4]. The advantage of coherent detection methods is that it is possible to record not only the intensity, but also a time-resolved amplitude of the electric field: a time series. In turn this leads to the possibility of obtaining a spectrum by Fourier transformation of the time domain signal, and opens up a wealth of spectroscopic analytic techniques, including those that rely on measuring changes in the phase of the measured signal.

In parallel with the development of pulsed techniques, work has been undertaken in the development of continuous wave terahertz imaging [5, 6], which allows precise tuning to a particular frequency. As monochromatic radiation is used the data acquired are simpler than in the pulsed case, and we shall not be considering these systems and the corresponding data further in this chapter. Advances have also led to the design of compact free-electron laser systems [7].

Terahertz-pulsed imaging is a development of terahertz time domain spectroscopy [8, 9, 10]. These workers have had success in measuring, in the terahertz band, the dielectric and optical properties of a range of materials including water, polar, and nonpolar liquids, gases, semiconductors and dielectrics. Terahertz-pulsed imaging involves projecting broadband pulses at a sample and either detecting them after transmission through the sample (transmission-based imaging) or detecting their reflections (reflection-based imaging). In the extension to imaging, the spectroscopic response of a sample is mapped by recording the transmitted or reflected broadband terahertz pulse at a series of contiguous pixel locations [11, 12]. The simplest images are generated by acquiring data at only one time point during the pulse, and plotting the amplitude of the signal at that time. Potentially more useful images can be generated by calculating parameters associated with the full time series at each pixel, and displaying those values using color look up tables [13]. Selected parametric terahertz-pulsed images of a wax-embedded melanoma section of thickness 1 mm, which has been prepared with the standard techniques used in histopathology, are shown in Plate V. The melanoma is outlined in the photograph in Plate V(a). The terahertz-imaged section was 7 mm ∗ 7 mm corresponding with the lower right quadrant of the photograph. The numerical values associated with the color scale are different for each of (b), (c), and (d).

The images shown in Plate V were acquired using the technique as it was introduced in 1995. Since that time, workers have introduced alternative acquisitions designed to improve one or more aspects of the measurement. Many of these are based on adaptation of mature algorithms from other fields. Darkfield imaging [14] was introduced to generate images where the image contrast arises from the differential scattering or diffraction of radiation. An alternative approach to diffraction imaging has been developed [15], with the emphasis on solution of the inverse problem to predict the aperture shape responsible for a measured diffraction field. Extraction of information about the location of buried structures was first obtained in 1997 [16], using time-of-flight reflection measurements analogous to B-mode ultrasound. In addition to generation of slice images in a plane perpendicular to the object surface, knowledge of depth of objects of interest allows spectroscopic measurement to be made only from the relevant location or the reconstruction of a slice parallel to the surface. The technique is most appropriate for objects where both negligible dispersion and absorption can be assumed. This assumption is not applicable to biomedical subjects, and led to the use of techniques from two related fields. Retaining a reflection geometry, techniques from geophysics have been applied leading to estimates of thickness and refractive index [17]. In contrast, by using a transmission geometry, the filtered back projection methods that underpin medical imaging techniques such as x-ray computed tomography have been applied to parametric projection images and the reconstruction of strong interfaces successfully demonstrated [18].

In spite of the increasing complexity of data acquisition, all the techniques retain a feature in common that sets them apart from other imaging methods. The data acquired consist of a time series rather than a single value, and new image analysis techniques are needed to ensure that all the information present is used. In our own area of interest, because the depth of penetration in human tissue is of the order of millimeters [19] it is likely that the first practical human in vivo imaging will involve data acquired in reflection, with transmission techniques being reserved for imaging of samples in vitro. While in the latter case it may be possible to simplify the geometry by sample preparation, in the former, unknown and complex tissue arrangements are expected.

There has been only limited work on applying computer vision techniques to terahertz images. Some [13] have suggested using specific "display modes" for certain applications, for example, ensuring that parameters are calculated from the part of the spectrum corresponding with absorption lines of particular molecules, and the range of parameters available for display was illustrated by others [20]. The first application of multidimensional classification techniques to terahertz data has also been described [21]. Mittleman et al. [22] introduced the idea of using wavelet-based techniques, and this idea was taken up by others [23, 24] for pulse denoising. We return to the topic of computer vision in terahertz imaging in Section 9.1.3, and introduce our own work in this field.

9.1.1 Equipment for Terahertz Pulsed Imaging

A schematic layout of a transmission terahertz-pulsed imaging system is shown
in Figure. 9.1. The technique is based on the pump- and probe-technique of op-
tical spectroscopy. An ultrafast infrared laser beam, giving femtosecond pulses,
is split in two. One part is used as the pump beam to generate picosecond
terahertz pulses, whilst the other forms part of the coherent detection system
and is used as a probe beam to detect the amplitude of the terahertz electric
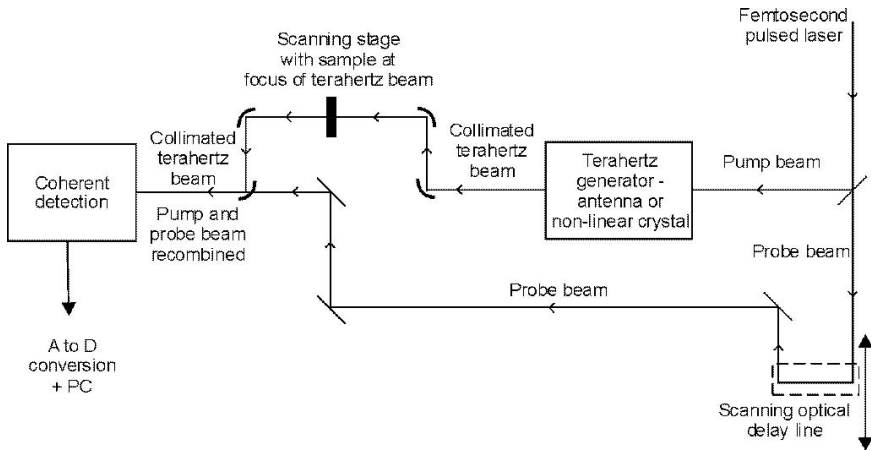field after it has interacted with the sample or subject.

Figure 9.1. Schematic layout of a transmission terahertz-pulsed imaging system.

There are two commonly used techniques for generating the pulses of ter-
ahertz radiation using the pump beam. In one, a voltage-biased photoconduc-
tive antenna [25] is illuminated with pulses from the ultrafast infrared laser.
Alternatively, the technique of optical rectification or optical mixing, may be
used to yield pulses containing frequencies up to 70 THz, which cross the bor-
der between the terahertz band and the far infrared. The infrared pulses are
used to illuminate a crystal with high nonlinear susceptibility [4, 26]. The re-
sulting terahertz beam is directed onto the sample or subject using parabolic
mirrors. The transmitted terahertz pulse profile is measured at a discrete
number of time points by scanning using an optical delay stage. The spatial
scanning of the object for image formation may most simply be performed
using raster scanning of either the terahertz beam or of the sample itself, but
this is time consuming. Alternative, faster, schemes are under development.
A promising method involves the illumination by the pump beam of a larger
area representing many pixels; a multielement array detector such as a charge
coupled device is used for detection [12, 27, 28]. More complete descriptions
of terahertz imaging systems are available [29].

Many of the systems in use for research are laboratory-based and occupy an area of up to $3\,\mathrm{m} * 2\,\mathrm{m}$, but more compact and portable systems are under development. An example is shown in Figure 9.2 which is a commercially available reflection system for use in dermatology. The box shown is $100\,\mathrm{cm}$ $\times$ $60\,\mathrm{cm}$ $\times$ $100\,\mathrm{cm}$ in size. The subject of interest is placed on a window on the top of the instrument, or examined using the probe attachment.

Figure 9.2. The TPI Scan$^{\mathrm{(TM)}}$: A complete terahertz imaging system including near-infrared laser and terahertz imaging optics for imaging biological tissue. Courtesy of TeraView Ltd, Cambridge, UK.

In Figure 9.3, a commercially available system is shown, which can be used in both reflection and transmission modes [30, 17].

A further system is under development by the Zomega Technology Corporation.

9.1.2 Potential Applications

In addition to the possibility of characterizing materials by spectroscopy, the penetration characteristics of terahertz radiation have also guided researchers towards potential applications. For example, polar liquids absorb strongly in the terahertz band; an example of such a liquid is water. Metals are opaque to terahertz radiation, whilst non-metals such as plastics and paper products are transparent, as are non-polar substances. Dielectrics have characteristic absorption features peculiar to each material. The exploitation of these penetration characteristics is discussed in more detail in the following sections.
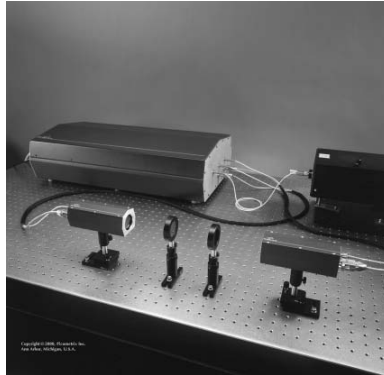
Figure 9.3. The Picometrix T-Ray$^{(TM)}$ 2000, the first commercial time domain terahertz spectroscopy and imaging system. Courtesy of Picometrix, Inc., Ann Arbor, MI.

Biomedical Imaging Applications

Our particular interest is in biomedical applications for terahertz imaging. The perceived advantages of using the terahertz band for biomedical applications include its sensitivity to the presence of water which may be of use for detecting or characterizing disease state, the lack of a hazard from ionization, relatively less Rayleigh scattering than for infrared and visible radiation, and the possibility of characteristic "signatures" from different tissues in health and in disease [31, 32, 33]. These characteristic signals may result from water content or other chemical features related to the composition or functional properties of the tissues.

- *Sensitivity to water*: An excellent example of utilization of the sensitivity of terahertz frequency radiation to the presence of water molecules is a study concerning the noninvasive continuous measurement of leaf water content [22, 34]. The technique may find further applications in agriculture and manufacturing [35], for assessing the moisturizing effects of cosmetics, and characterizing the flow of water through engineered materials or tissues. There is potential for distinguishing healthy and diseased tissue by its water content, where it may also be possible to differentiate bound and free water molecules [36]. We return to this last point later. The drawback of the high attenuation of terahertz frequency radiation by water is the concomitant limited depth of penetration (up to a few millimeters). However, even without special devices to deliver and detect the radiation inside the body, there is still a number of promising applications that do not require the radiation to travel far compared with the aforementioned depth of penetration. There are hopes that terahertz frequency imaging will be of value for in vivo characterization of dermatological conditions, or the early diagnosis of tooth decay.

- *Safety issues*: In common with many of the more recent introductions for medical imaging (ultrasound, magnetic resonance imaging, infrared techniques) terahertz frequency radiation is free from the ionization hazard associated with x-rays and nuclear medicine techniques. There are published guidelines regarding safe exposures, for example [37]. These were based on measurements made using wavelengths under $10.6\,\mu$m and pulse durations over $1.4\,$ns [38] and it is believed that under those conditions the damage mechanism is thermal. However there is also the possibility of resonant absorption mechanisms and thermomechanical and thermochemical effects for pulses of the type used in terahertz-pulsed imaging, and work is underway to investigate this [39, 40]. We have estimated that skin exposure for current pulsed systems using electronic and optical generation methods, where the average power of each pulse is under a milliwatt, will give exposures that are well within the limits set in the guidelines [41]. It is likely that the more powerful systems, such as those based on free electron lasers, may carry with them a hazard associated with heating.
- *Rayleigh scattering*: As the amount of Rayleigh scattering decreases with the fourth power of the wavelength, it is expected that terhertz frequency radiation should be scattered less than visible and near-infrared frequencies, which would be advantageous for imaging. This has been borne out by experiment. In a direct comparison of imaging using terahertz and near-infrared pulses, higher image contrast was obtained using the terahertz pulse although the near-infrared pulse was of higher power [42]. The difference could be explained by wavelength-dependent scattering.
- *Characteristic tissue "signatures"*: In Fourier transform infrared (FTIR) spectroscopy the word "signature" describes the presence of a characteristic absorption peak at a particular wavelength, which indicates the presence of a specific molecular bond. In some vitro applications for terahertz pulsed imaging, particularly of pure samples, signatures of this kind may be present. For the reasons outlined below we do not expect to see a single characteristic spectral absorption feature associated with each tissue in terahertz-pulsed imaging in vivo, or of tissue samples in vitro. Instead, we hypothesize that spectra from different tissues will have different shapes (or signatures), perhaps best described by a combination of absorption characteristics. The reason we do not expect to see sharp absorption peaks in spectra from tissues is because the samples will contain a complex mixture of several molecules. For each molecule, there may be several chemical environments, which will lead to smoothing of the spectral features. Finally, the presence of water, with its strong absorption, will potentially mask the other molecular absorptions.
- *Proposed biomedical applications*: Many applications have been proposed, ranging from studies at the genetic level, for example, investigating the hybridization state of DNA [43] to in vivo measurements of the thickness of skin [36]. Two Europe-wide projects are leading work in this field: first, Terahertz Bridge (http://www.frascati.enea.it/THz-BRIDGE/) which is

following a streamline of increasing complexity from biomolecules to cell membranes, cell nuclei, and tissues, and, secondly, Teravision (http://www.teravision.org) concentrating on imaging of intact tissue in vitro and in vivo.

Imaging, and computer vision, is most likely to be used for in vivo applications where knowledge of the spatial distribution of the chemically specific spectroscopic measurements is of value. A number of groups have demonstrated image contrast between tissues, though using, in general, very small numbers of samples. These demonstrations include data from pork and chicken [32, 31, 44, 45, 14], human tooth enamel and dentine [46], human skin in vivo [36], Spanish Serrano ham [24], histopathologically prepared human liver [47], and canine tumor [14]. A study of healthy tissue that includes repeated measurements from dehydrated tooth samples from seven individuals and freshly excised tissue samples from two donors has been reported [19]. The first study to include more samples in both health and disease, and thus having a higher power for hypothesis testing, is that of [48]. They imaged 15 samples of human healthy tissue and basal cell carcinoma.

These early results have led to optimism that early dental caries and skin cancers may be detectable using terahertz-pulsed imaging. Although there are alternative modalities that can be applied to each application, none has the necessary high sensitivity and specificity [49]. Other suggestions for terahertz-pulsed imaging include in vivo imaging of breast tumors, based on promising results obtained using microwaves [50] and in vitro results from terahertz-pulsed imaging [23]. Wound healing is an area attracting much interest, as terahertz imaging offers the potential of a noncontact measurement technique that could be used through a dry dressing.

Nonbiomedical Imaging Applications

- *Security and military applications*: These applications take advantages of the chemical specificity of the technique, and terahertz imaging has been advocated for remote scanning for biological agents such as anthrax or explosives [51]. Ranging studies to simulate radar of larger objects have been performed using terahertz radiation and scale models [52], and non-imaging versions of the technology are expected to have applications in communications.
- *Quality control*: Most packaging materials are transparent to terahertz radiation, so terahertz radiation has been proposed as a nonionizing substitute for quality control using x-rays in several industries including the food and textile industries. The connections in packaged integrated circuits may be assessed [22].
- *Characterization of semiconductors, gas identification*: Semiconductor characterization has been a particularly fertile area because dielectrics have a characteristic absorption dependent on the polarity and optical phonon

resonances peculiar to that material. Gas identification at terahertz frequencies [53] is also a good application because the emission and absorption lines of rotational and vibrational excitations of lighter molecules are strong in that part of the spectrum. Spectral lines are generally sharper in gaseous than in solid or liquid states, and this makes possible the precise localization of gas emission or the characterization of combustion flames.

- *Research applications*: The nondestructive and noncontact nature of the radiation has attracted the interest of those wishing to investigate valuable artifacts. There are potential uses for studying fossils in paleontology, visualizing through the surface layers of art works and other antiquities, and determining the content of books without the need to touch or disturb delicate pages.

Reviews that describe potential applications, with an emphasis on the biomedical, include those by Mittleman et al. [22] and Koch [54]. Siegel [55] gives a complete historical overview, including the passive imaging methods that are used for applications in astronomy and Anderton et al. [56] consider military applications.

9.1.3 Terahertz-Pulsed Imaging and Computer Vision

Terahertz-pulsed imaging presents challenges to analysis because in the acquired data set, each pixel contains a time series representing the measured terahertz frequency pulse. We have investigated some novel data processing approaches.

Time–Frequency Analysis

The aim in terahertz-pulsed imaging is to extract useful comparisons between a well-understood reference pulse, and those detected after transmission or reflection. Figure 9.4 shows three pulses — a reference pulse and two different transmission responses, one from nylon and one from cortical bone. Figure 9.5 shows these pulses after Fourier transformation. Notice that the spectra are very different, as are the pulses; they capture some of the information about the pulses that is obvious. For example, the high-frequency (noise) activity in the reference, and the reduced activity, or "power" in the transmitted pulses. However, features which, to the human eye, are dominant, such as the pulse delay, cannot be seen in this representation.

In order to describe the different overall shapes and characteristic absorption features that characterize the different materials, analysis of waveforms is usually based on Fourier decomposition [57]. Most of the applications listed in Section 9.1.2 have used analyses of this type. For example, Kindt and Schmuttenmaer [10] present a series of plots showing the refractive index and linear absorption coefficient of polar liquids plotted against frequency. On its own, however, Fourier transformation is somewhat crude since the measure is global
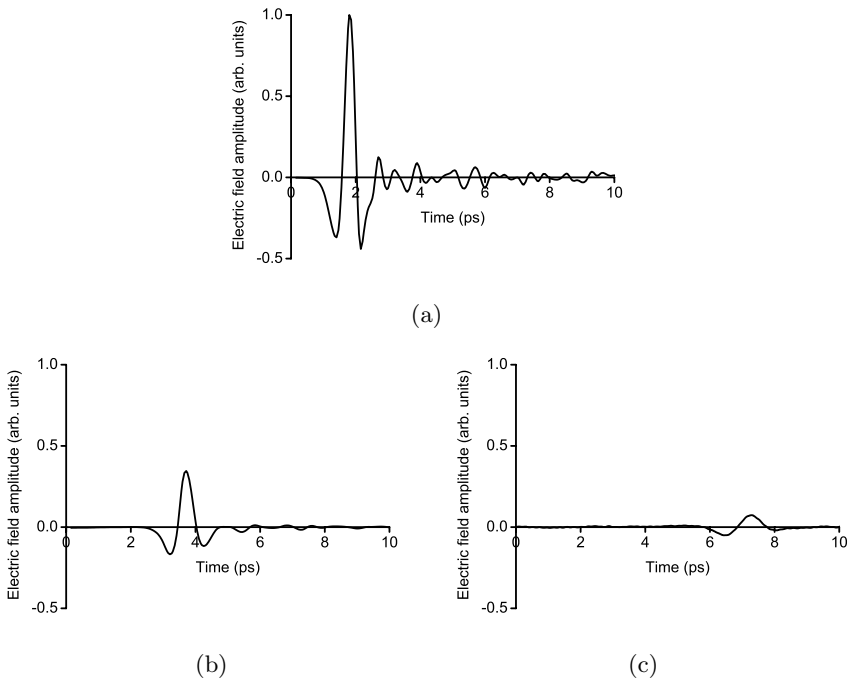
Figure 9.4. Three terahertz pulses. **(a)** A reference pulse. **(b)** The pulse after transmission through 1 mm of nylon. **(c)** The pulse after transmission though 1 mm of cortical bone.

to the signal. We seek mechanisms for deriving more local, time-specific, features. This is of particular importance for data comprising a series of pulses, at different times, representing interactions with different boundaries. The work in this chapter uses transmission data, from a single layer of material. Figure 9.4 illustrates that the reference pulse peak suffers a delay (along the time axis) and a flattening, or spreading, that are characteristic of the particular part of the sample under inspection. Ordinary Fourier transforms do not capture the time-dependent qualities of the information. There are also noticeable effects in the remainder of the signal that can be perceived as changes to the frequency make-up, which are dependent on the temporal instant. For example, the broadening of the main pulse suggests that the higher frequencies are no longer present, due to absorption, reflection or scattering, as they are responsible for the sharpness of the peak. It is hard to say, however, if the higher frequencies have been removed from the pulse uniformly over time.

An analytic technique was required that would perform the frequency space decomposition that Fourier transforms provide, but in a time-dependent manner. We have applied two approaches, the short-time Fourier transform and wavelets. The theoretical bases for these approaches are described in Sec-
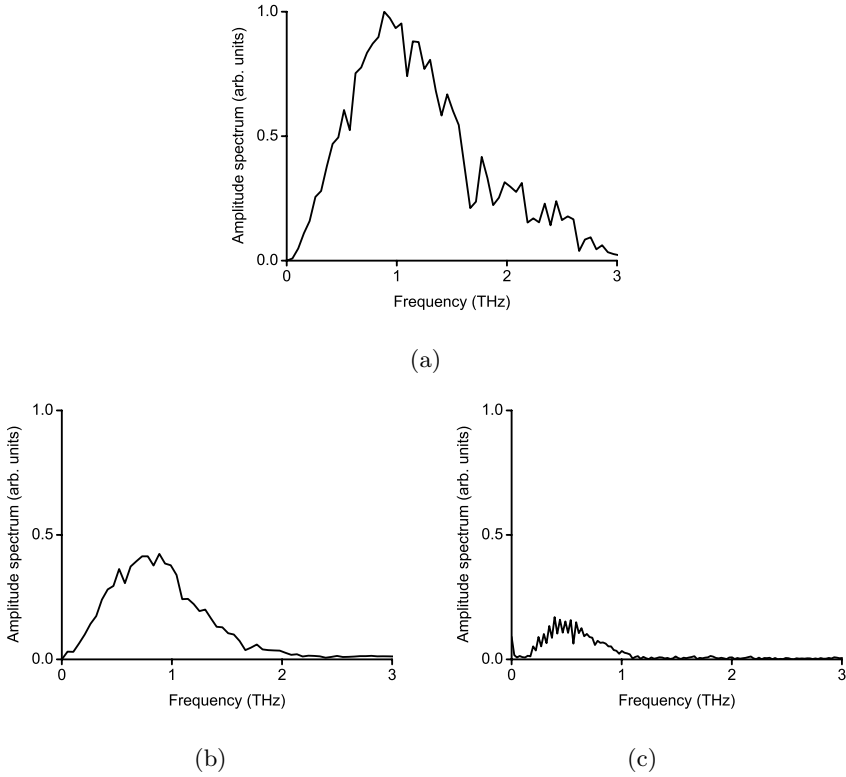
(a)

(b)   (c)

Figure 9.5. Frequency domain representation of three terahertz pulses. **(a)** A reference pulse. **(b)** The pulse after transmission through 1 mm of nylon. **(c)** The pulse after transmission though 1 mm of cortical bone.

tions 9.2.1 and 9.2.2. Wavelets were first used for terahertz imaging by Mittleman et al. [22], and have been used in other areas of biomedical signal processing [58, 59]. The techniques can generically be described as time-frequency techniques.

We have investigated the use of time-frequency techniques in two ways. The first of these would, in a generalized framework for computer vision [60]. be described as a segmentation task. Previous time-frequency segmentation work in biomedicine has been performed on breast RF data and on neurophysiological signals [61, 62]. For the terahertz data, both conventional and time-frequency methods were used to determine the refractive index and absorption coefficient of samples of nylon and resin, and the results compared. The second application is an example of a preprocessing or signal processing step. Time-frequency techniques have been applied for noise reduction of the acquired time series, following work on related modalities [63, 64, 65] and for compression. Compression may be required because very large data sets can

result from the need for spectroscopic detail at high spatial resolution. The effect of compression was determined by calculating the refractive index and absorption coefficient of nylon with and without compression. The refractive index and absorption coefficient of a material are key factors for terahertz-pulsed imaging. They determine the amplitude and timing of a transmitted, reflected or propagated pulse. Most parameters used for parametric images are strongly related to one or other property.

Clustering

In general, terahertz-pulsed imaging data are not amenable or accessible to the customary image processing and computer vision approaches unless these 3D data are first reduced, by the production of parametric images, to the two or three spatial dimensions used by such algorithms. However, workers in FTIR spectroscopy have reported successes with the analysis of complex samples by applying classification techniques to the acquired spectra [66]. This appears to be a promising approach for the terahertz frequency spectra we expect from tissue. They used prior knowledge of cellular structure in normal tissue and in the presence of carcinoma. The latter state is characterized by absence of particular cells, e.g., absence of goblet and mucin from colorectal adenocarcinomas, which has an effect on the shape of the spectrum. Classification success using training data, but without prior knowledge of biology, has recently been reported for terahertz imaging data [21].

Clustering methods fall into the category of segmentation in computer vision [60]. Here, image classification using clustering techniques (both for the full time series and for parameters derived from it) was applied to several terahertz images. These included a synthetic image with a known true classification, an acquired image where a classification was available from another imaging modality, and acquired images without knowledge of the true classification.

High-Level Processes

Higher-level processes used in computer vision, such as shape representation and shape extraction via motion, texture, etc., will be relevant for the analysis of parametric images or for classified images. Such analysis is not presented here. The ultimate aim of any computer vision analysis route is to extract "understanding" of some description from the data being processed. The understanding in biomedical terahertz imaging will be highly specific. Examples include the identification of regions of low mineralization representing early tooth decay, and associating different regions of an image with states of health and disease.

Thus, the purpose of this work was to apply data processing methods designed to suit the nature of terahertz-pulsed imaging data:

- To compare time-frequency techniques with conventional Fourier methods for extracting optical properties of materials.
- To determine the maximum degree of wavelet compression that would lead to no significant alteration in measured optical properties.
- To demonstrate clustering by multi-dimensional techniques.

In the following section we present a brief theoretical overview to support the methods that are described in Section 9.3.

9.2 Theory

9.2.1 Short-Time Fourier Transform (STFT)

The Fourier series representation of a real valued periodic function $f(t)$, with period T (so $f(t + T) = f(t)$) has Fourier series representation

$$f(t) \;=\; \sum_{-\infty}^{\infty} a_k e^{ik\omega t}, \tag{9.1}$$

where $\omega = 2\pi/T$ is the *fundamental frequency* and the Fourier coefficients are given by

$$a_k \;=\; \frac{1}{T} \int_{t_0}^{t_0+T} f(t)e^{-ik\omega t}dt. \tag{9.2}$$

This representation provides a decomposition of the function into frequency harmonics, whose contribution is given by the coefficients a_k. This decomposition is of great use in the analysis of functions since it betrays many useful properties; for example, very sharp changes contribute very high harmonic information, while slow variation is associated with low harmonics. Similarly, noise effects are often characterized by high frequency components.

More generally, for a nonperiodic function, the Fourier transform of $f(t)$ is given by

$$\hat{f}(\omega) \;=\; \int_{-\infty}^{\infty} f(t)e^{-i\omega t}dt. \tag{9.3}$$

This transform may be inverted, where $\hat{f}$ and f are a Fourier transform pair, by

$$f(t) \;=\; \frac{1}{2\pi} \int_{-\infty}^{\infty} \hat{f}(\omega)e^{i\omega t}d\omega. \tag{9.4}$$

However, the Fourier transform, and Fourier methods generally, are global, in the sense that they operate on the whole period of a function. In (9.2) we need full knowledge of $f(t)$ in order to extract the coefficients, and all values of $f(t)$ contribute to them. Any perturbation of $f(t)$ at any point will affect all the a_k. This leaves it of limited value when the effects under scrutiny are local, in the sense that there are time dependencies in the frequency content

of the signal. This is very much the case in the study of terahertz data — for example, in Figures 9.4(b) and 9.4(c), it is clear that the major peak of the pulse has been delayed, but by different lengths of time. The lack of information on time delays is evident in Figure 9.5. While it is possible to use the Fourier transform to estimate time delays by determining the phase difference between two pulses, the estimates tend to be inaccurate. The transform is a periodic function with 2π phase increments concealed by the periodicity, and inaccuracies arise from the limitations of the phase unwrapping algorithm used to estimate time delay. We seek, therefore, a combination of time and frequency analyses to permit the extraction of local effects using the power of the Fourier approach. This can be done by extracting windows of the original function before performing the Fourier analysis — this is the approach of the short-time Fourier transform. The simplest way to extract windows from a function is to multiply it by another function, such as a rectangular window of width 2τ, described by (9.5).

$$
\begin{aligned}
f_b(t) &= f(t)\varPhi(t - b) \\
&= \begin{cases} f(t) & t\epsilon[b - \tau, b + \tau] \\ 0 & \text{otherwise.} \end{cases}
\end{aligned}
\tag{9.5}
$$

The value of $f_b(t)$ can then be subjected to Fourier analysis in the normal manner.

The short-time Fourier transform (STFT) of the function $f(t)$ with respect to the window function $\varPhi(t)$ calculated at the frequency ξ and the time β is then

$$
G_\varPhi f(\beta, \xi) = \int_{-\infty}^{\infty} f(t)\varPhi(t - \beta)e^{-i\xi t}dt.
\tag{9.6}
$$

Contrast this with (9.4); we have added a second variable β to locate the transform in time. This is sometimes written, using the bar notation for the complex conjugate, as

$$
G_\varPhi f(\beta, \xi) = \int_{-\infty}^{\infty} f(t)\overline{\varPhi_{\beta,\xi}(t)}dt,
\tag{9.7}
$$

where

$$
\varPhi_{\beta,\xi}(t) = \varPhi(t - \beta)e^{i\xi t}.
\tag{9.8}
$$

It should be clear that the rectangular window function (9.5) is not best chosen for our purpose; the hard limiting step edges will cause any subsequent Fourier transform to include high-frequency components that are properties of the step rather than of the function. For this reason it is more common to use smooth window functions such as Gaussians. In particular, the Gabor transform uses the window function

$$
g_\alpha(t) = \frac{1}{2\pi\alpha}e^{t^2/4\alpha}
\tag{9.9}
$$

for some $\alpha > 0$.

In this work, we have used a simple Gaussian window (parameterized by its standard deviation) in all applications of the STFT. Applications of the STFT to two of the pulses of Figure 9.4 are in Figure 9.6. It can be seen that, in addition to the reduction in power, the transform has successfully captured the delay in the information in the transmitted pulse, at each frequency.
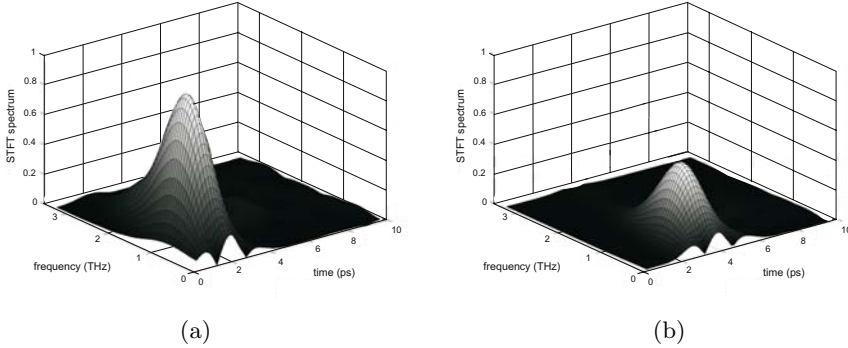

(a)   (b)

Figure 9.6. The STFT applied to: **(a)** the pulse of Figure 9.4(a) and **(b)** the pulse of Figure 9.4(b).

It is important to realize that it is impossible simultaneously to obtain good time resolution and good frequency resolution. Imagine a box drawn on a time-frequency graph, a narrow tall box has good time but poor frequency resolution, while a short wide one has bad time but good frequency resolution. The uncertainty principle determines the minimum area of this box, and thereby the usefulness of the technique. Conversely, the fact that the function is windowed permits real-time application of the STFT (since only limited information is needed), although this advantage is not relevant in this application. Various other transforms, which we will not consider here , exist with the aim of localizing the study of frequency, in particular the Wigner Ville transform [67]. The theory of Fourier transforms and series in discrete and continuous forms is described exhaustively elsewhere [68], and their application to signal and image processing is similarly fully described in other texts [60].

9.2.2 Wavelets

Wavelets overcome the shortcomings of the STFT by providing a basis for function representation that varies in frequency and time (translation). Where a number of STFT calculations would be required to include a range of window sizes in both frequency and time, this is achieved in a single wavelet operation.

This basis is derived from a mother function $\Psi(t)$ which is dilated (scaled) and translated to construct the family of basis functions. We write

$$\Psi_{b,a}(t) \;=\; \frac{1}{\sqrt{a}}\Psi\left(\frac{t-b}{a}\right) a \tag{9.10}$$

so a has the effect of dilating, or scaling, Ψ, and b translates.

These effects are illustrated in Figure 9.7 for a very simple mother function, the Haar. The scaling parameter a is clearly influencing the frequency of the function $-\frac{1}{a}$ is a measure of frequency.

(a)

(b)

(c)

(d)
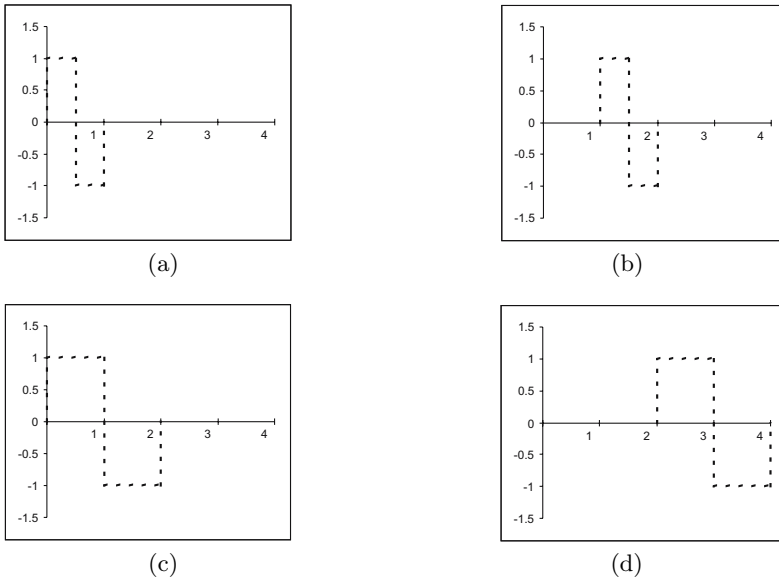
Figure 9.7. The Haar mother function with **(a)** a = 1, b = 0; **(b)** a = 1, b = 1; **(c)** a = 2, b = 0; **(d)** a = 2, b = 1.

Given this family of basis functions, we can now represent an arbitrary function $f(x)$ by correlating it with the scaled and translated versions of the mother. The continuous wavelet transform of $f(x)$ with respect to the mother $\Psi(t)$ is given by

$$W_\Psi f(b,a) \;=\; \int_{-\infty}^{\infty} f(t)\overline{\Psi_{b,a}(t)}dt. \tag{9.11}$$

A wavelet transform of the terahertz pulse of Figure 9.4(b) is shown in Figure 9.8. Notice the degree of detail here; wavelet representations can be difficult to interpret without practice and concentration, however, as for Figure 9.6, it is straightforward to observe the time delay of the high-frequency component.
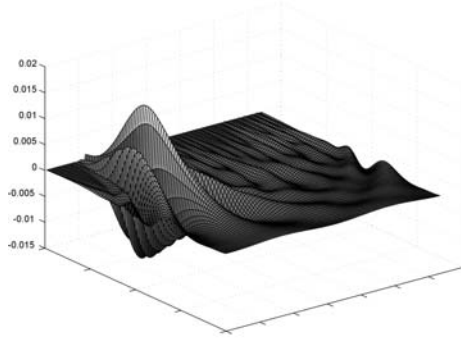
Figure 9.8. The Morlet wavelet transform of the terahertz pulse in Figure 9.4(b). The scale axis runs from front to back, and the time (or translation) axis from left to right.

The wavelet transform is invertible, provided

$$\hat{\Psi}(0) \;=\; 0 \tag{9.12}$$

where $\hat{\Psi}$ is the Fourier transform of Ψ – (9.4). To recapture f, a two-dimensional integration over both parameters a and b is required;

$$f(t) \;=\; \frac{1}{C_\Psi} \int_{-\infty}^{\infty} \int_{-\infty}^{\infty} \frac{1}{a^2} [W_\Psi f(b, a)] \Psi_{b,a}(t) da db. \tag{9.13}$$

Here C_Ψ is a constant dependent on the mother, given by

$$C_\Psi \;=\; \int_{-\infty}^{\infty} \frac{|\hat{\Psi}(\omega)|^2}{\omega} d\omega. \tag{9.14}$$

We require this constant to be finite. This is known as the admissibility condition that restricts the class of functions that may be chosen as wavelets. Note in particular that of necessity $\hat{\Psi}(0) = 0$.

The functions f we observe are of course discrete, and so require a discretized continuous wavelet transform in the same manner as a discrete Fourier transform is defined. In fact, the continuous transform contains a lot of redundancy; this, together with the computational load of a simple discretization, has led to the development of very efficient subsamplings to provide the discrete wavelet transform (DWT). This is normally done by taking the scale parameter a to be of the form 2^s for an integer s, and $b = k2^{-s}$. Then, (9.11) becomes

$$W_\Psi f(k2^{-s}, 2^{-s}) \;=\; 2^{s/2} \int_{-\infty}^{\infty} f(t) \Psi(2^s t - k)(t) dt. \tag{9.15}$$

If F is discretized, with a sampling rate chosen as 1 for convenience, this becomes

$$W_\Psi f(k2^{-s}, 2^{-s}) \;=\; 2^{s/2} \sum_n f(n)\Psi(2^s n - k). \qquad (9.16)$$

Note that in computing this, we only need to know the function values where the corresponding wavelet value is nonzero.

9.2.3 Computer Vision Background

Wide-Band Cross-Ambiguity Function, WBCAF

Significant relevant theory on signal pulses was developed in the study of radar, in which we are often interested in correlating a signal with time-shifted copies of itself. The aim is to extract time delay and Doppler shift, thereby making good estimates of signal delay, and implicitly distance of travel [67]. The relevant ambiguity function of a signal is given by

$$A_f(\xi, x) \;=\; \int_{-\infty}^{\infty} f\left(b + \frac{x}{2}\right) \overline{f\left(b - \frac{x}{2}\right)} e^{-i\xi b} db. \qquad (9.17)$$

The transforms in which we are interested perform a correlation of the observed data with individual basis functions, not with itself. The wide-band cross-ambiguity function, WBCAF [69], of a function $f_2(t)$ against a reference $f_1(t)$ is defined as

$$WBCAF_{f_1} f_2(\tau, \sigma) \;=\; \frac{1}{\sqrt{\sigma}} \int_{-\infty}^{\infty} f_2(t) \overline{f_1 \frac{t - \tau}{\sigma}} dt, \qquad (9.18)$$

where f_1 has been delayed by τ and scaled by σ. This permits the extraction of the appropriate τ (time delay) for each scale σ, by locating the value of τ that provides the maximum value of correlation at that σ.

Note, however, the similarity between (9.11) and (9.18). The WBCAF resembles the continuous wavelet transform, using the reference function as the wavelet mother. This is an expensive computation, since the reference f_1 needs repeated resampling (interpolation, filtering, subsampling), which can generate a prohibitive overhead. To overcome this, Young [70] has developed the wavelet-based wide-band cross-ambiguity function

$$WB - WBCAF_{f_1} f_2(\tau, \sigma) \;=\; \int_{-\infty}^{\infty} \int_{-\infty}^{\infty} W_\Psi f_2(a, b) \overline{W_\Psi f_1\left(\frac{a}{\sigma}, \frac{b - \tau}{\sigma}\right)} \frac{da\, db}{a^2},$$
$$\qquad (9.19)$$

where W_Ψ is the continuous wavelet transform with respect to the mother Ψ. Using an arbitrary mother permits efficient precomputation of the wavelets for all relevant τ and σ

The WB-WBCAF permits useful measurements to be made on an output pulse. Fixing the scale at 1, determining the translation which provides the maximal response gives a good estimate of the time delay associated with the pulse. This measurement, which may be considered as a cross-correlation or

the application of a matched filter, provides the parameter that gives the best match with the reference. Note that we cannot determine the time delay as easily at different scales, since the scaling operation also causes a shift in the reference. We can normalize the WB-WBCAF and the WBCAF using (9.18) at various values of σ

$$\frac{MAX_\tau(WBCAF_{f_1}f_2[\tau, \sigma])}{MAX_{\tau'}(WBCAF_{f_1}f_1[\tau', \sigma])}. \tag{9.20}$$

This parameter, which we shall call the WBCAF absorption, can then be taken to be proportional to the relative transmission of the band of frequencies corresponding to scale σ. The reasoning here is that $WBCAF_{f_1}f_2(\tau, \sigma)$ is the spectral content of f_2 with respect to f_1 at σ and τ, while similarly $WBCAF_{f_1}f_1(\tau', \sigma)$ is the spectral content of f_1. It is necessary to use different values of τ because the pulses experience different time delays, and must first be aligned in time to ensure that the WBCAF absorption is calculated using the same part of each pulse. Finding the maximum value of the WBCAF in τ achieves this. The ratio of these two should then give the power ratio of f_1 to f_2 at that σ.

Compression

The task of data compression has been approached via function transforms in many ways [60]. At their simplest, the coefficients of a function's Fourier transform are often negligibly small (corresponding to harmonics that scarcely appear in the function). One approach to compression is to derive a far more compact representation of the transform by neglecting these coefficients. The inverse Fourier transform of this compressed transform will then provide a good approximation to the original function, since the information lost is insignificant.

The same approach may be taken with the wavelet transform, where a similar observation may be made about coefficients of small magnitude. Figure 9.9 shows a histogram of the frequency of occurrence of values of the wavelet coefficients for the terahertz pulse in Figure 9.4(b). It is clear that the majority of these are relatively insignificant. Wavelet compression could be achieved by setting the smallest value coefficients to zero.

Clustering

Multidimensional data are often easily represented by clusters. The centers (usually centroids) of these clusters may then be used as exemplars. If the exemplars are indeed good examples of the data clustered around them, a highly compact codebook representation of the data becomes available. Terahertz imaging datasets can be interpreted as large, high-dimensional vectors; at their simplest, each "pixel" (time series) can be taken as a vector of length
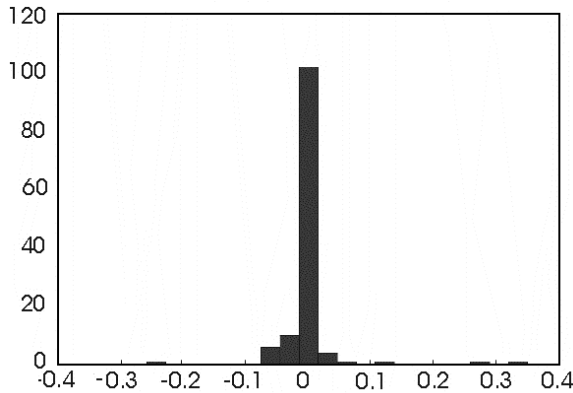
Figure 9.9. The frequency of occurrence of values of the wavelet coefficients for the terahertz pulse in Figure 9.4(b).

equal to the number of time samples it provides. Each vector is then termed a "feature." Alternatively, we might look for clustering of other features derived from the pulses, such as Fourier or wavelet coefficients. A clustering of these vectors might then seek out physical similarities in the sample under inspection. Clustering has received much attention in the literature. The simplest approach (and widely used) is the k-means algorithm [71], which may be summarized as the following

1. Select N, the number of clusters to be formed.
2. Choose initial cluster centers v_1, v_2, ..., v_N.
3. Determine for each data point its closest "center."
4. Recalculate centers as centroids of allocated data points.
5. Iterate from step 3 until no change.

It should be clear that this algorithm may be applied generally to any multi-dimensional data. It has been the subject of significant work, in particular to determine favorable values for N, and the initialization v_1, v_2, ..., v_N [72].

9.2.4 Transmission of Terahertz Radiation

In this work we have assumed the following simple model for the transmission of the terahertz pulses.

Refractive Index

When considering the time delay caused by transmission through a thickness x of material, compared with transmission through the same distance in vacuo. Let the velocity in vacuo be c, and in the medium v. Then the difference in

time taken by radiation following the two paths, $\Delta t = (x/v - x/c)$. But the refractive index n, is defined as $n = c/v$, so

$$\Delta t = x(n-1)/c. \tag{9.21}$$

Thus, if the time delay is measured for a range of sample thickness, n can be found from the slope of a plot of Δt against x. The true refractive index of a material varies with frequency, but the single value found by this technique is a single broadband measurement and will be peculiar to the system on which measurements were made.

Absorption Coefficient

The absorption of a beam of radiation of incident intensity I_0, transmitted through a thickness x, is described by the Beer–Lambert law,

$$\frac{I}{I_0} = e^{-\mu x} \text{ or } \ln\left(\frac{I}{I_0}\right) = -\mu x \tag{9.22}$$

where μ is the linear absorption coefficient. If scattering is considered to be negligible, a plot of $\ln(I/I_0)$ against x is linear with slope $-\mu$, as for a given material and with the simple geometry of the samples used here, reflection losses will be constant and do not affect the slope of the graph. The Beer–Lambert expression was used in the time domain to give an estimate of the broadband absorption coefficient. In this work we also apply it in the frequency domain to give the absorption coefficient as a function of frequency, and in the STFT and WBCAF analyses. In the latter cases the relevant linear absorption coefficient is derived by replacing I/I_0 with an estimate of maximum transmittance (over t or τ) derived from the STFT or WBCAF; in the case of the WBCAF this is defined by (9.20).

9.3 Methods

9.3.1 Optical Properties of Materials

We wanted to use samples whose optical properties were known not to vary with time, and in spite of our interest in biomedical applications, this ruled out the use of tissue samples. The acquisition time was long enough for tissue samples to dehydrate and change the values we were trying to measure. So specially manufactured test objects were used instead. Two step-wedges were manufactured by rapid prototyping [73]. One, from nylon (Duraform polyamide, nylon 12) by the selective laser sintering process. The other made of resin by stereo-lithography. The test objects had steps of known thickness ranging from 0.1 mm to 7 mm and are shown in Figure 9.10.

Transmission data were acquired from both step wedges, using the pulsed terahertz imaging system at JW Goethe-Universität, Frankfurt. The time series recorded at each pixel comprised 128 points, separated by 0.15 ps for the nylon step wedge and at 0.2 ps for the resin step wedge. Parametric images representing the step wedge data are shown in Figure 9.11.
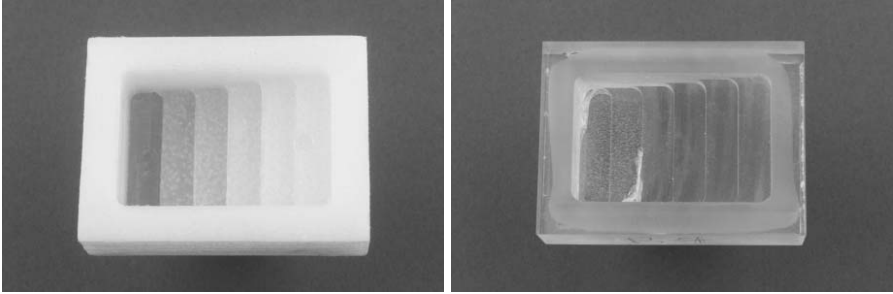

Figure 9.10. Nylon (left) and resin (right) step wedges. Each block measures approximately $4\,cm \times 3\,cm \times 1\,cm$.

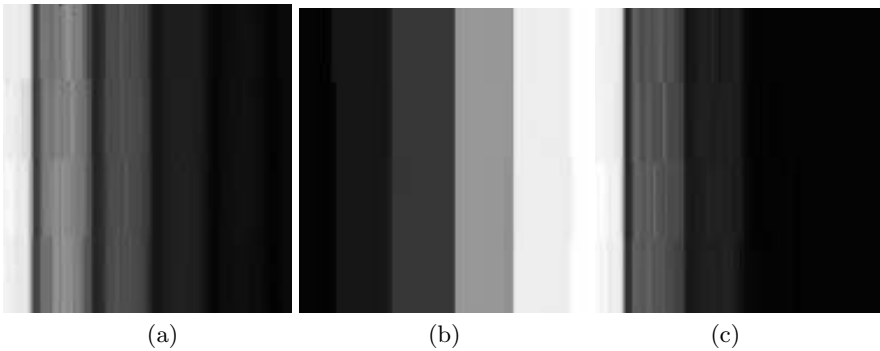(a)   (b)   (c)

Figure 9.11. Parametric terahertz-pulsed images taken from the nylon step wedge data set. The white end of the gray scale represents large values, and as in Figure 9.12 the thinnest step is at the left. **(a)** Pulse amplitude relative to reference pulse amplitude, in time domain. **(b)** Time delay between transmitted pulse peak and peak of reference. **(c)** Transmittance (ratio of transmitted and incident intensities after Fourier transformation of pulses) at 1.2 THz.

Refractive Index, Broadband, and as a Function of Frequency

Two methods for finding the broadband refractive index were used — the conventional time domain analysis and the WBCAF analysis. STFT analysis

was used to find the variation of refractive index with frequency. For the conventional analysis, the time delay was estimated for each pixel in the time domain. For the wavelet-based analysis, the WBCAF was calculated at scale 1, and the time delay was the value of τ that maximized the correlation (9.18). For the STFT analysis, the STFT was performed using a Gaussian window of width 1.5 ps. For each frequency, the time delay was the time at which the value of the STFT was a maximum. In each case, the mean value for the time delay was found within a region of interest, approximately $40 * 40$ pixels, one in each step. Time delay was plotted against step depth, and the refractive index was found using (9.21). The standard error of the slope was calculated.

Attenuation: Broadband and as a Function of Frequency or Scale

For each material, a region of interest approximately $40 * 40$ pixels was defined in each step of the wedge.

1. A broadband estimate of transmittance was made, using the square of the measured peak amplitude in the time domain I/I_0. These results were plotted against step thickness and (9.22) used to calculate the broadband linear absorption coefficient
2. Following Fourier transformation, the transmittance $I(\omega_i)/I_0(\omega i)$ was calculated at several values of frequency. At each frequency, (9.22) was used to calculate the linear absorption coefficient, and these results were plotted against frequency.
3. Following short-time Fourier transformation, the maximum transmittance, $\max_t(I(\omega_i)/I_0(\omega_i))$ was calculated at several values of frequency. At each frequency, this value was substituted for I/I_0 in (9.22), and was used to calculate the STFT linear absorption coefficient. These results were plotted against frequency.
4. Equation (9.20) was used to calculate the proposed WBCAF-absorption at 13 values of scale. At each scale, this value was substituted for I/I_0 in (9.22), and was used to calculate the WBCAF linear absorption coefficient. These results were plotted against scale.

In each case the standard deviation of the linear absorption coefficient was determined from the plot against step thickness. The results of the analyses were not directly comparable because the wavelet-based technique gives results in terms of scale rather than frequency, but it was possible to inspect the plots of absorption parameters to gain a qualitative impression of their ability to discriminate between materials.

9.3.2 Signal Compression

The conventional calculations to determine the refractive index and absorption coefficient associated with the nylon step wedge, described in Section 9.3.1, were repeated using a range of reduced versions of the wavelet transform.

These reductions were compressions of the transform data obtained by setting to zero the smallest (in magnitude) $p\%$ of coefficients, before performing the calculations. This common form of compression does not, of course, result in the data requiring $(100 - p)\%$ space, since the resulting sparse arrays require indexing information to locate the surviving coefficients. Nevertheless, given that we experimented with values of p in excess of 50, the potential for compression of the (real valued) data is clear.

The quality of the results generated was easy to assess in the case of the refractive index; taking the uncompressed transform data as a gold standard, a simple numerical comparison permitted an evaluation of the result extracted from the compressed form. The absorption coefficient measurement was generated at a range of terahertz frequencies. These results were compared with those from the uncompressed data by calculating the Pearson correlation coefficient (measuring the degree of linear relationship between data sets), the root mean square difference, and Student's paired t-test probability, which provides a confidence estimate for a set of pairs of observations being matching pairs [74].

9.3.3 Clustering Demonstrations

Synthetic Image of Tooth Slice

Our first experiment on clustering was designed to determine the importance of initialization on the success of the classification, and to compare various choices of feature vector. We used a synthetic image data set because in that case the class of each pixel is known, and this can be used to determine the success of the classification. A $50 * 50$ pixel image of a slice of a tooth was generated. Each pixel was set to belong to one of three classes comprising tooth enamel, tooth dentine, and air, and these were distributed in a realistic configuration by tracing the outlines from an image of a tooth slice. This is illustrated in Figure 9.12(a). A typical time series for each material was taken from a real data set, and noise was modeled by adding normally distributed noise, with values selected at random from the distribution, to each time point of the time series at each pixel. The noise was taken from a single Gaussian distribution; the mean of the distribution was taken from inspection of time series from the background of the real image, and the standard deviation chosen empirically. The validity of this noise model is discussed in Section 9.5. In this preliminary experiment partial volume effects were not incorporated into the model. Three parametric images representing the synthetic data are shown in Figures 9.12(b)–(d).

The number of clusters was set to three, representing air, enamel, and dentine, and standard k-means clustering with random initialization was used [75]. Four different feature vectors were used: for 1–3 the vector dimension was 64 or 128 depending on the number of time samples in the data:
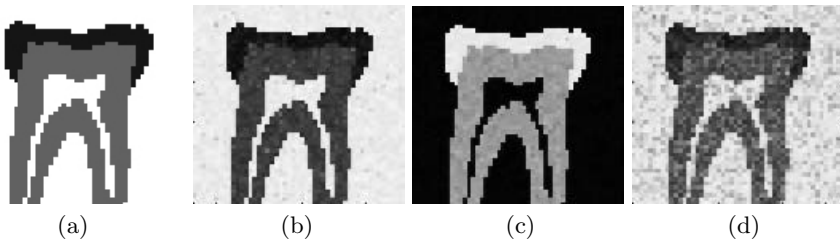
1. The time series.

| (a) | (b) | (c) | (d) |

Figure 9.12. (a) Allocation of classes in the synthetic image of a tooth slice. Black represents enamel, gray dentine, and white air. **(b)–(d)** Parametric terahertz-pulsed images taken from the synthetic data set. **(b)** Pulse amplitude relative to reference pulse amplitude, in time domain. **(c)** Time delay between transmitted pulse peak and peak of reference. **(d)** Transmittance (ratio of transmitted and incident intensities after Fourier transformation of pulses) at 0.85 THz.

2. Fast Fourier transform (FFT) of time series.
3. Discrete wavelet transform (DWT) of time series.
4. A three dimensional vector using three parameters calculated from the time series. These were the integral phase shift between 0.5 and 1 THz, the integral phase shift between 1 and 1.5 THz and the absorbance $A = -\log_{10}(I/I_0)$ at 1 THz. The three parameters were normalized to be univariate within a unit hypercube to ensure that differences in units between them did not bias the outcome.

The result of using random initialization was, as expected, that many classifications were "unsuccessful," for example, many of the air pixels were wrongly classed as enamel or dentine, or where only two classes resulted. Future work will concentrate on refining the initialization, but for these initial experiments we simply repeated each classification several times, and termed it "successful" if the result was three contiguous regions broadly occupying the relevant locations. For each "successful" classification the number of misclassified pixels in the image was determined as a percentage of the total number of pixels.

Terahertz-Pulsed Image of Tooth Slice

The same methods of classification were used on a nonsynthetic image of a dehydrated tooth slice of thickness approximately $200\,\mu$m. Transmission data were acquired from an area $22.2\,$mm $* 9\,$mm, using the pulsed terahertz imaging system at the University of Leeds. The image array was $56 * 56$ pixels, and the time series recorded at each pixel comprised 64 points separated by $0.15\,$ps. Three parametric images representing the tooth data are shown in Figure 9.13.

Unlike the synthetic tooth data, there are no known classes for this data. To allow the results to be assessed against an independent modality we acquired a radiograph of the tooth slice using a dental x-ray system operating
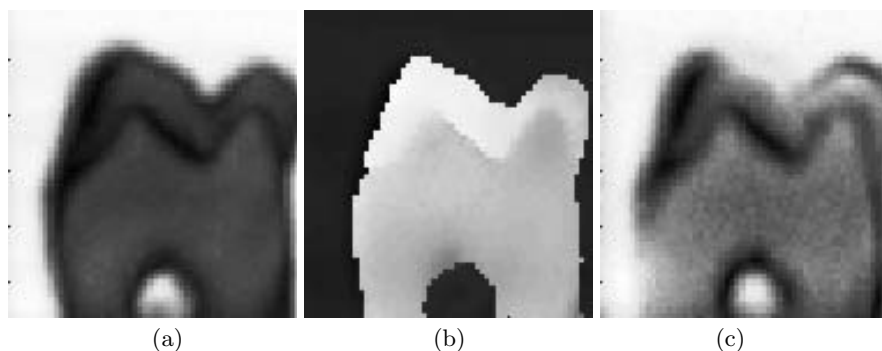
(a)   (b)   (c)

Figure 9.13. Parametric terahertz-pulsed images taken from the tooth slice data set. **(a)** Pulse amplitude relative to reference pulse amplitude, in time domain. **(b)** Time delay between transmitted pulse peak and peak of reference. **(c)** Transmittance (ratio of transmitted and incident intensities after Fourier transformation of pulses) at 0.85 THz.

at 60 kV. Using a commercial biomedical image processing package (Analyze, AnalyzeDirect.com, Lenexa, Kansas, USA), this image was registered to a parametric image derived from the terahertz-pulsed image data. Interactive region growing was used to define the enamel, dentine, and air regions on the registered x-ray image. These definitions were used to produce an outline that was overlaid on the clustering results, to give a visual indication of the accuracy of the classification. The percentage of misclassified pixels was determined. Further quantification was not attempted because the tooth slice was not of perfectly uniform thickness, being thinner at the top right, and this would lead to errors in the classification based on automatic clustering.

Terahertz-Pulsed Images of Histopathological Samples

Classification techniques were run on two further data sets. In these cases unregistered optical images were available for comparison, and it is important to note that clinically important differences will not necessarily be seen in the photograph. The image data sets were acquired from wax embedded histopathologically prepared sections of tissue, of thickness 1 mm. The preparation involved dehydration and fixing with formalin, and this means that terahertz radiation was able to penetrate the tissue more readily than would be the case if the tissue were fresh. Transmission data were acquired from both, using the pulsed terahertz imaging system at the University of Leeds. The first example was of basal cell carcinoma and the second melanoma. In each case the time series recorded at each pixel comprised 64 points separated by 0.15 ps. For the basal cell carcinoma the image array was $56 * 56$ pixels over an area $10 \, \text{mm} * 10 \, \text{mm}$, for the melanoma the image array was 20 by 18 pixels over an area $5 \, \text{mm} * 4.5 \, \text{mm}$.

k-means clustering on the fast Fourier transform coefficients of the time series was applied to the basal cell carcinoma data, using five and eight classes. For the melanoma, the fast Fourier transform coefficients were again used, this time with both k-means clustering and vector quantization, each for five classes. Three parametric images representing the basal cell carcinoma and melanoma histopathological data are shown in Figure 9.14.
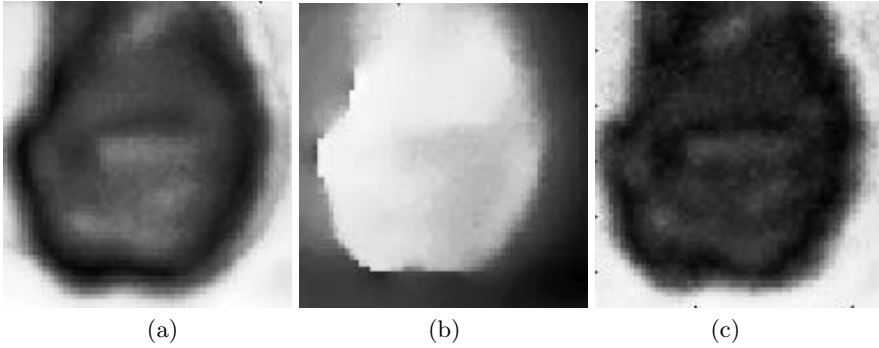

(a) (b) (c)

Figure 9.14. Parametric terahertz-pulsed images taken from the histopathological basal cell carcinoma (top) and melanoma (below) data sets. **(a)** Pulse amplitude relative to reference pulse amplitude, in time domain. **(b)** Time delay between transmitted pulse peak and peak of reference. **(c)** Transmittance (ratio of transmitted and incident intensities after Fourier transformation of pulses) at 2 THz.

Matlab (Version 6, The MathWorks, Inc., Cambridge, UK) was used for the post-acquisition image and signal analysis work described in this section.

9.4 Results

9.4.1 Optical Properties of Materials

Refractive Index: Broadband and as a Function of Frequency

Results for the broadband refractive index are shown in Table 9.1, and the variation of refractive index with frequency from the STFT analysis is in Figure 9.15. It can be seen that the refractive index decreases with increasing frequency, and is higher for resin than for nylon, which is consistent with the broadband results.

These results illustrate that any image reconstruction algorithm requiring an assumption of negligible dispersion would be valid for nylon but not for resin.

Table 9.1. Results of refractive index measurements, mean ± standard deviation

	Nylon	Resin
Conventional time domain	1.603 ± 0.004	1.66 ± 0.01
WBCAF at scale 1	1.597 ± 0.005	1.64 ± 0.02
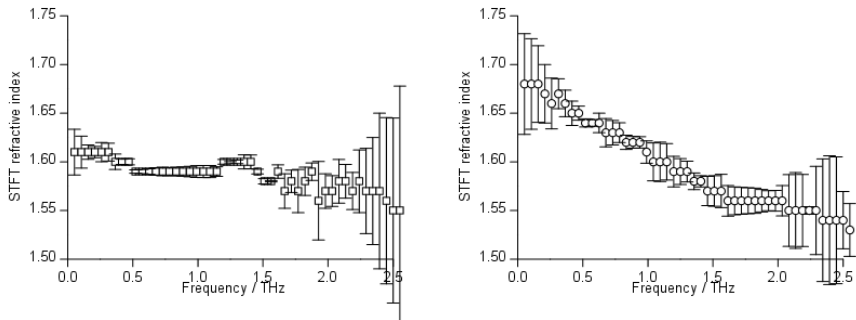
Figure 9.15. STFT refractive index against frequency for nylon (left) and resin (right). Error bars show ± one standard deviation.

Attenuation: Broadband and as a Function of Frequency

From the conventional broadband analysis, for nylon the linear absorption coefficient was $6.8 \pm 0.5\,\mathrm{cm}^{-1}$ and for resin $11.8 \pm 1.6\,\mathrm{cm}^{-1}$. Figure 9.16(a) shows the variation of linear absorption coefficient with frequency, using conventional Fourier analysis. The two materials may be differentiated throughout the frequency range by their linear absorption coefficient. Figure 9.16(b) shows the variation of the STFT linear absorption coefficient with frequency. As was the case for the conventional Fourier analysis the two materials may be differentiated throughout the frequency range by their STFT absorption coefficient. The values diverge with increasing frequency as the curves diverge for the conventional analysis, but the analysis is robust to a higher frequency. This is likely to be a consequence of the windowed nature of the transform, and suggests that the STFT may be valuable for analysis of noisy data such as that acquired from tissue in our system between 1.5 and 2.5 THz.

Figure 9.17 shows the variation of the WBCAF linear absorption coefficient with frequency. As was the case for the conventional Fourier analysis the two materials may be differentiated throughout the scale range by their WBCAF absorption coefficient, which is higher for resin than for nylon. The values diverge as the scale decreases, which corresponds with the way in which the curves diverge with increasing frequency for the conventional and STFT analyses. For nylon, the WBCAF linear absorption coefficient is almost constant with scale, in contrast to the behavior with frequency of the linear absorption coefficient calculated both by conventional methods and using the STFT.
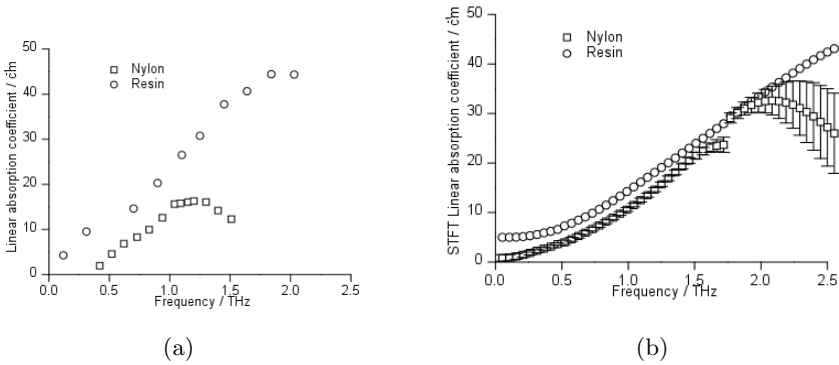
(a)   (b)

Figure 9.16. (a) Conventional Fourier analysis to show the variation of the linear absorption coefficient with frequency **(b)** STFT analysis to show the variation of the STFT linear absorption coefficient with frequency. The error bars have been omitted from the resin STFT data points — they were of approximately the size of the symbol, where shown they represent ± one standard deviation.

Thus, for some materials, reconstruction methods that require an assumption of negligible changes in absorption with frequency could appropriately be tackled using a wavelet approach.
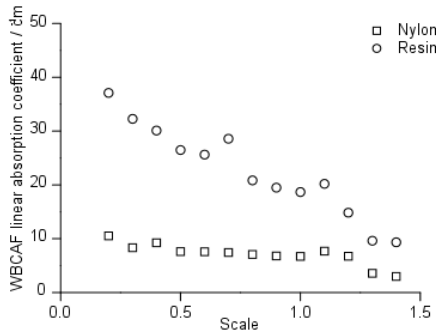

Figure 9.17. Results of WBCAF analysis to show the variation of the WBCAF linear absorption coefficient with scale.

9.4.2 Signal Compression

Refractive Index

Compression to very high levels has a negligible impact on the broadband refractive index calculations (Table 9.2). This measurement is robust until 90%

Table 9.2. Broadband refractive index, n, for different compression levels.

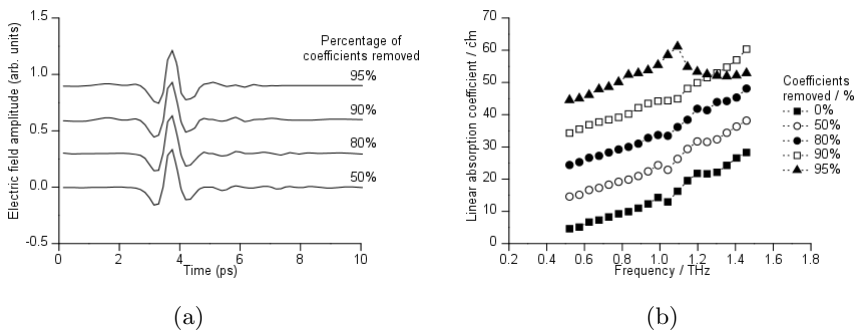| Coefficients removed / %	0	50	80	90	95
n	1.603	1.603	1.604	1.603	1.61
Standard deviation of n	0.002	0.002	0.003	0.005	0.01

(a)   (b)

Figure 9.18. (a) The terahertz pulse of Figure 9.4(b) transmitted through 1 mm of the nylon step-wedge compressed by removal of 50%, 80%, 90%, and 95% of the smaller coefficients. The pulses are shown offset in the amplitude direction for clarity. **(b)** Linear absorption coefficient against frequency for nylon using conventional Fourier analysis, at various degrees of wavelet compression. To allow comparison, the results for the various degrees of compression have been offset from the uncompressed result at intervals of $10 \, \text{cm}^{-1}$.

of the coefficients are removed, at which point a small error is introduced. The terahertz pulse of Figure 9.4(b) is shown in Figure 9.18 reconstructed from the discrete wavelet transform after the truncation of 50%, 80%, 90%, and 95% of the smaller coefficients. As expected, the major feature of the pulse (the main peak) is unaffected, while the truncation removes more and more of the smaller scale features, which we might expect to be largely noise.

Absorption Coefficient

The results of the statistical tests of similarity between the uncompressed and compressed observations across a range of frequencies from 0.52 to 1.46 THz at intervals of 0.05 THz, for various truncations, are shown in Table 9.3. Figure 9.18(b) shows the absorption coefficient at selected frequencies, for various truncations. More detailed results are presented elsewhere [76]. Up to about 1 THz, the curves coincide. However, note that the spectral feature at 1.1 THz is lost when 90% of the coefficients are removed, and significant errors appear at 95%. The statistical tests all suggested that there is no significance in the differences as far as 10% compression (90% of the coefficients are removed),

the global nature of the statistic masked the disappearance of a local feature, which could be of importance.

Table 9.3. Results of statistical tests comparing absorption coefficient cm^{-1} at various degrees of compression.

Coefficients removed / %	0%	50%	80%	90%	95%
Pearson correlation	1.0	0.999	0.997	0.992	0.495
RMSD	0	0.09	0.61	0.97	7.05
P (paired t)	—	0.43	0.85	0.40	0.06

9.4.3 Clustering

Synthetic Image of Tooth Slice

Clustering performed on the synthetic tooth image produced promising results. Table 9.4 records the percentage of misclassified pixels as a result of clustering the entire pulse data, the FFT of the pulse data, the DWT, and a 3D feature vector. The high quality of these results is partly because the issue of initialization was not addressed. The basic k-means algorithm is very susceptible to initialization, and some runs produced very poor results that were simply excluded in these experiments. We have not yet experimented with more intelligent initialization procedures, but once this is done we would expect results approaching this quality.

Table 9.4. Percentage of misclassified pixels: Tooth slice.

Synthetic image of tooth slice	% misclassified
Time series	0
FFT coefficients	0.04
DWT coefficients	0
Feature vector	1

Terahertz-Pulsed Image of Tooth Slice

Results for the image of the $200\,\mu$m tooth slice are presented in Table 9.5.

Figure 9.19 illustrates classifications resulting from time series, FFT, and feature-vector clustering. The pulse relative amplitude image is shown as an indicator of where physical boundaries in the sample lie. The boundaries segmented from the radiograph are shown in white as an overlay.

Table 9.5. Percentage of misclassified pixels: Tooth slice.

Terahertz pulsed image of tooth slice	% misclassified
Time series	19
FFT coefficients	23
DWT coefficients	19
Feature vector	13

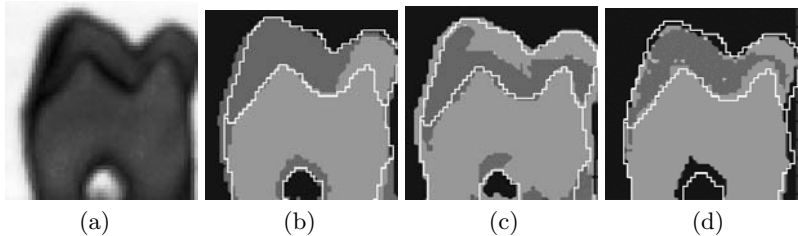
(a)   (b)   (c)   (d)

Figure 9.19. The tooth slice data set. **(a)** Parametric terahertz-pulsed image show-
ing pulse amplitude relative to reference pulse amplitude, in time domain. **(b)** Result
of clustering using the whole time series in the time domain. **(c)** Result of clustering
using the FFT coefficients. **(d)** Result of clustering using the 3D feature vector. In
(b)–(d) air is shown in black, enamel in dark gray, and dentine in light gray. The
white outline indicates the boundaries of dentine and enamel that were identified
interactively on the radiograph of the tooth slice.

Terahertz-Pulsed Images of Histopathological Samples

Results from performing clustering on the hisopathological data sets are shown
in Figures 9.20 and 9.21. For the basal cell carcinoma data a feature is em-
phasized in white at the center of Figure 9.20(b) which is not apparent in
the photograph. As stated previously, one does not expect clinically impor-
tant features necessarily to be obvious in the photograph. The feature is also
evident in the transmittance terahertz image shown earlier in Figure 9.14(c),
but use of the FFT coefficients in the clustering has defined it more clearly.

For the melanoma data set the classes returned by the two types of cluster-
ing differ. Again they do not correspond with the regions of the photograph,
nor were they expected to. The mid-gray feature shown by clustering using
the FFT coefficients in Figure 9.21(b) is also apparent to a lesser extent in
each of the parametric images in Figure 9.14.

9.5 Discussion

Terahertz-pulsed imaging is a relatively new modality that records large datasets
that are difficult to visualize. Conventional Fourier and time domain tech-
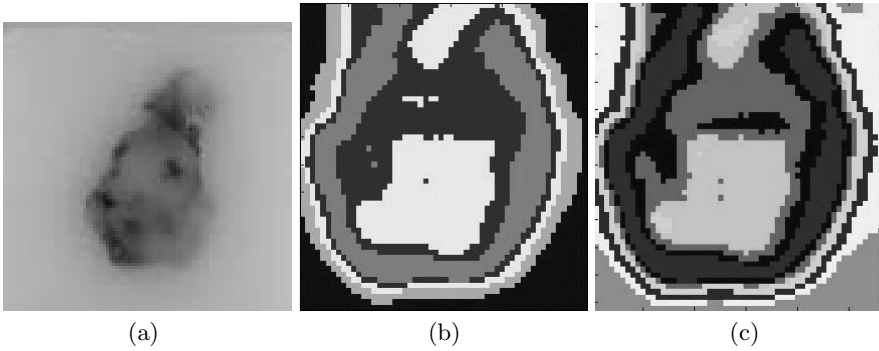niques are widely used for analysis, but there is no standardization on the

<center>(a)   (b)   (c)</center>

Figure 9.20. The basal cell carcinoma data set. **(a)** Photograph showing the histopathologically prepared sample. **(b)** Result of clustering into five classes using the using the FFT coefficients. **(c)** Result of clustering into eight classes using the using the FFT coefficients.
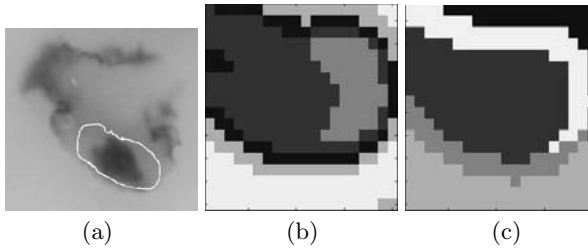

<center>(a)   (b)   (c)</center>

Figure 9.21. The melanoma data set. **(a)** Photograph showing the histopathologically prepared sample, with the melanoma outlined. The terahertz imaged area corresponds to the lower right quadrant of this photograph. **(b)** Result of k-means clustering into five classes using the using the FFT coefficients. **(c)** Result of vector quantization clustering into five classes using the FFT coefficients.

methods or presentation of data. A powerful addition to the analysis would be the ability to consider time and frequency independently, but this is not possible using the Fourier transform, so time-frequency techniques such as the STFT and wavelets have been considered. The limitations of the uncertainty principle on the STFT means that it would be necessary to run the analysis many times to get a complete picture of the variations with time and frequency. Wavelet analysis, although still constrained by the uncertainty principle, can give a more complete picture from a single analysis. Wavelet analysis has proved successful in related areas where analysis of time series is required, including ultrasound and radar. The analysis is particularly attractive for use with terahertz pulses because they can be described very efficiently by wavelets, where the Fourier transform is a less efficient basis. This is encouraging for applications such as compression and noise reduction, and may be an advantage in other analytical methods. Wavelet techniques

are also attractive experimentally, because there is an established theoretical background and robust software is available.

In this work we investigated a range of potential alternatives to conventional Fourier analysis. We have shown that, for our test materials, the STFT and wavelet analyses give, within experimental error, the same result for refractive index as the conventional method. The simple WBCAF analysis involves estimation of time delays only at scale 1 because changing the scale results in an associated time shift. Extension to higher scales is an area for future work. The absorption coefficients produced by conventional and wavelet analysis are not directly comparable, because the conventional analysis produces values at given frequencies, while the wavelet results are plotted against scale, each of which represents a range of frequencies. However, we see a similar pattern of differences between two materials in this simple case of transmission imaging, and believe that the opportunity to focus on particular time periods with wavelets will be helpful for more complex images. In addition, a material that showed increasing absorption coefficient with frequency by Fourier techniques demonstrated an almost constant WBCAF absorption coefficient with scale. This may be a property that could be exploited in reconstruction techniques that require an assumption of negligible variation in absorption with frequency . It is a limitation of the work presented here that only two materials were studied, and neither of these was biomedical. In such material, biological variation is expected, and the value of the optical parameters will vary from sample to sample [19]. Nor will tissue be neatly arranged as a step wedge, so a smaller number and range of thicknesses would be available. Adaptation of existing techniques for refractive index estimation, which have been successful for characterizing semiconductors [77, 78], will be needed.

An understanding of the imaging process is often fundamental to successful analysis of medical imaging data [79, 80]. There are still many factors that need to be included in the analysis, perhaps by including a model of the imaging process such as diffraction, scattering, pulse shape, partial volume effects, frequency dependent amplitude and frequency-dependent spatial resolution. It should also be possible to exploit models of how the pulses are expected to appear [81], especially with advances in pulse shaping [82].

In this work a very simple model of the noise in terahertz pulsed images was used when making the synthetic tooth data set. Recent analysis has shown that a single Gaussian does not correctly model the noise, and improving the noise model is an area of current research. These are very early results, but clearly do not rule out the use of time-frequency techniques in this field. The robust results from these initial experiments in the simplest case of using transmission data through a single layer give us confidence for applying adaptations of the methods to data where time localization will be important for identifying which pulse corresponds with which boundary.

The use of wavelets for signal compression is a well known application, and it would be of real practical benefit in terahertz pulsed imaging. Our initial work presented here has highlighted the difficulties associated with quantifying

the effect of such compression. Statistical tests showed no significant difference between pulses where, by eye, it could be seen that a potentially relevant spectral feature had been lost. Testing of the effect of compression is therefore application specific, and one must address the question of whether the final conclusion has been affected by the process. In our particular example, we sought changes to the measured values of refractive index, and in this case the loss of the spectral feature was not important. We suspect that this will not be the case when terahertz-pulsed imaging moves into clinical and laboratory use.

The idea of using clustering methods that use more of the information in the time series at each pixel than just two or three parameters is very attractive, and has been used successfully in other fields [66]. Our work here is very preliminary, and the next stage is to perform a study on large numbers of samples for which we have a gold standard classification by another technique, for evaluation. However, from these early results it appears that robust segmentation, using features derived from the terahertz pulses is a real possibility. The incorporation of knowledge about likely signal changes from particular disease processes could be built in to the classification scheme, and classified data may form the input for filtered back projection.

Terahertz-pulsed imaging is in its infancy, and in order to speed up the imaging process many of the early systems do not collect the whole time series at each pixel. Even when data from the whole pulse are available, users display or use parametric images for further calculation without an understanding of the most appropriate choice of parameter to emphasize a feature of interest. In this work, we have presented preliminary simple experiments to investigate techniques that made use of all the information in each pulse. The results from these justify further investigation in this area and our aim is to provide tools for the user that will optimize their use of the spectroscopic information hidden in each terahertz signal.

9.6 Acknowledgments

carried out x-ray imaging; J. Biglands performed additional software work; and G.C. Walker commented on the manuscript.

References

[1] Allen, S.J., Craig, K., Galdrikian, B., Heyman, J.N., Kaminski, J.P., Scott, J.S.: Materials science in the far-IR with electrostatic based FELs. Nuclear Instruments & Methods in Physics Research Section A; Accelerators Spectrometers Detectors and Associated Equipment **35** (1995) 536–539

[2] Jaroszynski, D.A., Ersfeld, B., Giraud, G., Jamison, S., Jones, D.R., Issac, R.C.: The Strathclyde terahertz to optical pulse source (TOPS). Nuclear Instruments & Methods in Physics Research, Section A: Accelerators Spectrometers Detectors and Associated Equipment **445** (2000) 317–31

[3] Grischkowsky, D.R., Mittleman, D.M.: Introduction. In Mittleman, D., ed.: Sensing with Terahertz Radiation. Springer-Verlag, Berlin (2003) 1–38

[4] Auston, D.H., Nuss, M.C.: Electrooptic generation and detection of femtosecond electrical transients. IEEE Journal of Quantum Electronics **24** (1988) 184–197

[5] Kleine-Ostmann, T., Knobloch, P., Koch, M., Hoffmann, S., Breede, M., Hofmann, M.: Continuous-wave THz imaging. Electronics Letters **37** (2001) 1461–146

[6] Siebert, K.J., Quast, H., Leonhardt, R., Loeffler, T., Thomson, M., Bauer, T.: Continuous-wave all-optoelectronic terahertz imaging. Applied Physics Letters **80** (2002) 3003–3005

[7] Gallerano, G.P., Doria, A., Giovenale, E., Renieri, A.: Compact free electron lasers: From Cerenkov to waveguide free electron lasers. Infrared Physics & Technology **40** (1999) 161–174

[8] Grischkowsky, D., Keiding, S., van Exter, M., Fattinger, C.: Far-infrared time-domain spectroscopy with terahertz beams of dielectrics and semiconductors. Journal of the Optical Society of America, B: Optical Physics **7** (1990) 2006–201

[9] van Exter, M., Grischkowsky, D.R.: Carrier dynamics of electrons and holes in moderately doped silicon. Phys. Rev. B **41** (1990) 12140–12149

[10] Kindt, J.T., Schmuttenmaer, C.A.: Far-infrared dielectric properties of polar liquids probed by femtosecond terahertz-pulse spectroscopy. Journal of Physical Chemistry **100** (1996) 10373–10379

[11] Hu, B.B., Nuss, M.C.: Imaging with terahertz waves. Optics Letters **20** (1995) 1716–171

[12] Wu, Q., Hewitt, T.D., Zhang, X.C.: Two-dimensional electro-optic imaging of THz beams. App. Phy. Lett. **69** (1996) 1026–1028

[13] Herrmann, M., Tani, M., Sakai, K.: Display modes in time-resolved terahertz imaging. Japanese Journal of Applied Physics, Part 1: Regular Papers, Short Notes & Review Papers **39** (2000) 6254–625

[14] Loeffler, T., Bauer, T., Siebert, K.J., Roskos, H.G., Fitzgerald, A., Czasch, S.: Terahertz darkfield imaging of biomedical tissue. Optics Express **9** (2001) 616–62

[15] Ruffin, A.B., Van Rudd, J., Decker, J., Sanchez-Palencia, L., Le Hors, L., Whitaker, J.: Time reversal terahertz imaging. IEEE Journal of Quantum Electronics **38** (2002) 1110–111

[16] Mittleman, D.M., Hunsche, S., Boivin, L., Nuss, M.C.: T-ray tomography. Optics Letters **22** (1997) 904–90

[17] Dorney, T.D., Symes, W.W., Baraniuk, R.G., Mittleman, D.M.: Terahertz multistatic reflection imaging. Journal of the Optical Society of America, A: Optics Image Science and Vision **19** (2002) 1432–144

[18] Ferguson, B., Wang, S.H., Gray, D., Abbot, D., Zhang, X.C.: T-ray computed tomography. Optics Letters **27** (2002) 1312–131

[19] Berry, E., Fitzgerald, A.J., Zinovev, N.N., Walker, G.C., Homer-Vanniasinkam, S., Sudworth, C.D.: Optical properties of tissue measured using terahertz-pulsed imaging. Proceedings of SPIE: Medical Imaging **5030** (2003)

[20] Loeffler, T., Siebert, K.J., Czasch, S., Bauer, T., Roskos, H.G.: Visualization and classification in biomedical terahertz-pulsed imaging. Physics in Medicine and Biology **47** (2002) 3847–3852

[21] Ferguson, B., Wang, S., Gray, D., Abbott, D., Zhang, X.C.: Identification of biological tissue using chirped probe THz imaging. Microelectronics Journal **33** (2002) 1043–105

[22] Mittleman, D.M., Jacobsen, R.H., Nuss, M.C.: T-ray imaging. IEEE Journal of Selected Topics in Quantum Electronics **2** (1996) 679–69

[23] Mickan, S., Abbott, D., Munch, J., Zhang, X., van Doorn, T.: Analysis of system trade-offs for terahertz imaging. Microelectronics Journal **31** (2000) 503–51

[24] Ferguson, B., Abbott, D.: De-noising techniques for terahertz responses of biological samples. Microelectronics Journal **32** (2001) 943–95

[25] Auston, D.H., Cheung, K.P., Valdmanis, J.A., Kleinman, D.A.: Coherent time-domain far-infrared spectroscopy with femtosecond pulses. Journal of the Optical Society of America A: Optics Image Science and Vision **1** (1984) 1278

[26] Zhang, X.C., Jin, Y., Hu, B.B., Li, X., Auston, D.H.: Optoelectronic study of piezoelectric field in strained-layer superlattices. Superlattices and Microstructures **12** (1992) 487–490

[27] Shan, J., Weling, A.S., Knoesel, E., Bartels, L., Bonn, M., Nahata, A.: Single-shot measurement of terahertz electromagnetic pulses by use of electro-optic sampling. Optics Letters **25** (2000) 426–42

[28] Ruffin, A.B., Decker, J., Sanchez-Palencia, L., Le Hors, L., Whitaker, J.F., Norris, T.B.: Time reversal and object reconstruction with single-cycle pulses. Optics Letters **26** (2001) 681–68

[29] Mittleman, D.M., ed.: Sensing with Terahertz Radiation. Springer-Verlag, Berlin (2003)

[30] Zimdars, D.: Commercial T-ray systems accelerate imaging research. Laser Focus World **37** (2001) 91

[31] Arnone, D.D., Ciesla, C.M., Corchia, A., Egusa, S., Pepper, M.: Applications of terahertz (THz) technology to medical imaging. Proceedings of SPIE **3828** (1999) 209–219 Terahertz Spectroscopy and Applications 11; JM Chamberlain (ed.).

[32] Mittleman, D.M., Gupta, M., Neelamani, R., Baraniuk, R.G., Rudd, J.V., Koch, M.: Recent advances in terahertz imaging. Applied Physics B-Lasers and Optics **68** (1999) 1085–109

[33] Smye, S.W., Chamberlain, J.M., Fitzgerald, A.J., Berry, E.: The interaction between terahertz radiation and biological tissue. Physics in Medicine and Biology **46** (2001) R101–R112

[34] Hadjiloucas, S., Karatzas, L.S., Bowen, J.W.: Measurements of leaf water content using terahertz radiation. IEEE Transactions on Microwave Theory and Techniques **47** (1999) 142–149

[35] Boulay, R., Gagnon, R., Rochette, D., Izatt, J.R.: Paper sheet moisture measurements in the far-infrared. International Journal of Infrared and Millimeter Waves **5** (1984) 1221–1234

[36] Cole, B.E., Woodward, R., Crawley, D., Wallace, V.P., Arnone, D.D., Pepper, M.: Terahertz imaging and spectroscopy of human skin, invivo. Commercial and Biomedical Applications of Ultrashort Pulse Lasers; Laser Plasma Generation and Diagnostics **4276** (2001) 1–10

[37] Institute, A.N.S.: American National Standard for Safe Use of Lasers (ANSI Z136.1 - 2000). Laser Institute of America, Orlando, FL (2000)

[38] Sliney, D.H., Wolbarsht, M.L.: Laser Safety Standards: Evolution and Rationale. Safety with Lasers and Other Optical Sources. Plenum Press, New York (1980)

[39] Clothier, R.H., Bourne, N.: Effect of THz exposure on human primary keratinocyte differentiation and viability. Journal of Biological Physics **29** (2003) 179–185

[40] Scarfi, M.R., Romano, M., Di Pietro, R., Zeni, O., Doria, A., Gallerano, G.P.: THz exposure of whole blood for the study of biological effects on human lymphocytes. Journal of Biological Physics **29** (2003) 171–176

[41] Berry, E., Walker, G.C., Fitzgerald, A.J., Chamberlain, J.M., Smye, S.W., Miles, R.E.: Do *in vivo* terahertz imaging systems comply with safety guidelines? Journal of Laser Applications **15** (2003) 192–198

[42] Han, P.Y., Tani, M., Usami, M., Kono, S., Kersting, R., Zhang, X.C.: A direct comparison between terahertz time-domain spectroscopy and far-infrared Fourier transform spectroscopy. Journal of Applied Physics **89** (2001) 2357–235

[43] Bolivar, P.H., Brucherseifer, M., Nagel, M., Kurz, H., Bosserhoff, A., Buttner, R.: Label-free probing of genes by time-domain terahertz sensing. Physics in Medicine and Biology **47** (2002) 3815–3821

[44] Bezant, C.D.: Application of THz Pulses in Semiconductor Relaxation and Biomedical Imaging Studies. PhD thesis, Department of Physics (2000)

[45] Han, P.Y., Cho, G.C., Zhang, X.C.: Time-domain transillumination of biological tissues with terahertz pulses. Optics Letters **25** (2000) 242–24

[46] Ciesla, C.M., Arnone, D.D., Corchia, A., Crawley, D., Longbottom, C., Linfield, E.H.: Biomedical applications of terahertz-pulse imaging. Commercial and Biomedical Applications of Ultrafast Lasers II **3934** (2000) 73–8

[47] Knobloch, P., Schildknecht, C., Kleine-Ostmann, T., Koch, M., Hoffmann, S., Hofmann, M.: Medical THz imaging: an investigation of histopathological samples. Physics in Medicine and Biology **47** (2002) 3875–388

[48] Woodward, R.M., Cole, B.E., Wallace, V.P., Pye, R.J., Arnone, D.D., Linfield, E.H.: Terahertz-pulse imaging in reflection geometry of human skin cancer and skin tissue. Physics in Medicine and Biology **47** (2002) 3853–3863

[49] Fitzgerald, A.J., Berry, E., Zinovev, N.N., Walker, G.C., Smith, M.A., Chamberlain, J.M.: An introduction to medical imaging with coherent terahertz frequency radiation. Physics in Medicine and Biology **47** (2002) R67–R8

[50] Hagness, S.C., Taflove, A., Bridges, J.E.: Two-dimensional FDTD analysis of a pulsed microwave confocal system for breast cancer detection: Fixed-focus and antenna-array sensors. IEEE Transactions on Biomedical Engineering **45** (1998) 1470–147

[51] Wang, S., Ferguson, B., Mannella, C., Abbott, D., Zhang, X.C.: Powder detection using THz imaging. In: Proceedings of Conference on Lasers and Electro-Optics, Long Beach, CA (2002) 132

[52] McClatchey, K., Reiten, M.T., Cheville, R.A.: Time-resolved synthetic aperture terahertz impulse imaging. Applied Physics Letters **79** (2001) 4485–448

[53] Jacobsen, R.H., Mittleman, D.M., Nuss, M.C.: Chemical recognition of gases and gas mixtures with terahertz waves. Optics Letters **21** (1996) 2011–201

[54] Koch, M.: Biomedical applications of THz imaging. In Mittleman, D., ed.: Sensing with Terahertz Radiation. Springer-Verlag, Berlin (2003) 295–316

[55] Siegel, P.H.: Terahertz technology. IEEE Transactions on Microwave Theory and Techniques **50** (2002) 910–928

[56] Anderton, R.N., Appleby, R., Borrill, J.R., Gleed, D.G., Price, S., Salmon, N.A. In: Prospects of Imaging Applications [Military]. IEE (1997) 4/1–4/10

[57] Papoulis, A.: The Fourier Integral and Its Application. McGraw-Hill, New York (1962)

[58] Akay, M., ed.: Time Frequency and Wavelets in Biomedical Signal Processing. IEEE Press and John Wiley & Sons (1998)

[59] Xu, X.L., Tewfik, A.H., Greenleaf, J.F.: Time-delay estimation using wavelet transform for pulsed-wave ultrasound. Annals of Biomedical Engineering **23** (1995) 612–621

[60] Sonka, M., Hlavac, V., Boyle, R.: Image Processing, Analysis and Machine Vision. second edn. Brooks/Cole Publishing Company, Pacific Grove, CA (1999)

[61] Georgiou, G., Cohen, F.S., Piccoli, C.W., Forsberg, F., Goldberg, B.B.: Tissue characterization using the continuous wavelet transform, part II: Application on breast RF data. IEEE Transactions on Ultrasonics Ferroelectrics and Frequency Control **48** (2001) 364–373

[62] Sun, M., Sclabassi, R.J.: Wavelet feature extraction from neurophysiological signals. In Akay, M., ed.: Time Frequency and Wavelets in Biomedical Signal Processing. IEEE Press and John Wiley & Sons (1998) 305–321

[63] Ching, P.C., So, H.C., Wu, S.Q.: On wavelet denoising and its applications to time delay estimation. IEEE Transactions on Signal Processing **47** (1999) 2879–2882

[64] Coifman, R.R., Wickerhauser, M.V.: Experiments with adapted wavelet de-noising for medical signals and images. In Akay, M., ed.: Time Frequency and Wavelets in Biomedical Signal Processing. IEEE Press and John Wiley & Sons, Piscataway, NJ (1998) 323–346

[65] Sardy, S., Tseng, P., Bruce, A.: Robust wavelet denoising. IEEE Transactions on Signal Processing **49** (2001) 1146–115

[66] Lasch, P., Naumann, D.: FT-IR microspectroscopic imaging of human carcinoma thin sections based on pattern recognition techniques. Cellular and Molecular Biology **44** (1998) 189–20

[67] Carmona, R., Hwang, W.L., Torresani, B.: Practical Time-Frequency Analysis. Academic Press, San Diego (1998)

[68] Gioswami J. C., Chan, A.K.: Fundamentals of Wavelets: Theory, Algorithms, and Applications. John Wiley and Sons, New York (1999)

[69] Weiss, L.G.: Wavelets and wideband correlation processing. IEEE Signal Processing Magazine **11** (1994) 13–32

[70] Young, R.K.: Wavelet Theory and Its Applications. Kluwer, Boston (1993)

[71] MacQueen, J.: Some methods for classification and analysis of multivariate observations. In: Proceedings of 5th Berkeley Symposium 1. (1967) 281–297

[72] Kaufmann, L., Rousseeuw, P.J.: Finding groups in data: An introduction to cluster analysis. John Wiley & Sons, New York (1990)

[73] Webb, P.A.: A review of rapid prototyping (RP) techniques in the medical and biomedical sector. Journal of Medical Engineering & Technology **24** (2000) 149–15

[74] Goulden, C.H.: Methods of Statistical Analysis. second edn. John Wiley and Sons, New York (1956)

[75] Hartigan, J.: Clustering Algorithms. John Wiley and Sons, New York (1975)

[76] Handley, J.W., Fitzgerald, A.J., Berry, E., Boyle, R.D.: Wavelet compression in medical terahertz-pulsed imaging. Physics in Medicine and Biology **47** (2002) 3885–389

[77] Duvillaret, L., Garet, F., Coutaz, J.L.: A reliable method for extraction of material parameters in terahertz time-domain spectroscopy. IEEE Journal of Selected Topics in Quantum Electronics **2** (1996) 739–74

[78] Dorney, T.D., Baraniuk, R.G., Mittleman, D.M.: Material parameter estimation with terahertz time-domain spectroscopy. Journal of the Optical Society of America, A: Optics Image Science and Vision **18** (2001) 1562–157

[79] Highnam, R., Brady, M.: Mammographic Image Analysis. Kluwer Academic Publishers, Dordrecht (1999)

[80] Cotton, S., Claridge, E., Hall, P.: Noninvasive skin imaging. Information Processing in Medical Imaging **1230** (1997) 501–50

[81] Duvillaret, L., Garet, F., Roux, J.F., Coutaz, J.L.: Analytical modeling and optimization of terahertz time-domain spectroscopy experiments using photoswitches as antennas. IEEE Journal of Selected Topics in Quantum Electronics **7** (2001) 615–62

[82] Lee, Y., Meade, T., Norris, T.B., Galvanauskas, A.: Tunable narrow-band terahertz generation from periodically poled lithium niobate. Applied Physics Letters **78** (2001) 3583–358